Journal of Power Sources 271 (2014) 489–496

Contents lists available at ScienceDirect

Journal of Power Sources

journal homepage: www.elsevier.com/locate/jpowsour

$K_{1-x}Fe_{2+x/3}(CN)_6 \cdot yH_2O$, Prussian Blue as a displacement anode for lithium ion batteries

Mª José Piernas-Muñoz [a], Elizabeth Castillo-Martínez [a, *], Vladimir Roddatis [a], Michel Armand [a], Teófilo Rojo [a, b, *]

[a] CIC Energigune, Parque Tecnológico de Álava, Albert Einstein 48, Ed. CIC, 01510 Miñano, Spain
[b] Departamento de Química Inorgánica, Universidad del País Vasco UPV/EHU, P.O. Box 664, 48080 Bilbao, Spain

HIGHLIGHTS

- Prussian Blue, $K_{0.88}Fe^{III}_{1.04}[Fe^{II}(CN)_6] \cdot yH_2O$, is used as anode in lithium ion batteries.
- It can deliver 450 mAh g^{-1} at 8.75 mA g^{-1} in the low voltage window from 0.005 to 1.6 V vs Li^+/Li.
- For the first time, a conversion or displacement reaction is proposed for this kind of systems.

ARTICLE INFO

Article history:
Received 20 June 2014
Received in revised form
1 August 2014
Accepted 5 August 2014
Available online 15 August 2014

Keywords:
Electrochemical energy storage
Prussian Blue
Anodes
Li-ion batteries
Displacement reaction
Conversion reaction

ABSTRACT

Nanosized Prussian Blue, $K_{0.88}Fe_{2.04}(CN)_6 \cdot yH_2O$, prepared in aqueous solution at room temperature, is shown to be active as anode for lithium ion batteries after mild dehydration. It exhibits reversible capacities of up to 400 mAh g^{-1} at 8.75 mA g^{-1} and 150 mAh g^{-1} at 1750 mA g^{-1}, with relatively low hysteresis and long cycle life in the low voltage range 0.005–1.6 V vs lithium. Ex-situ XRD, FTIR as well as SEM and TEM studies on pristine and cycled electrodes suggest that the reversible insertion of about ~5 Li^+/f.u. is associated with a displacement (or conversion) reaction on the Prussian Blue structure along with the reduction of all iron atoms, reported for the first time in this kind of systems. The products of re-oxidation do not recover the crystal structure of Prussian Blue.

1. Introduction

Lithium ion batteries are the most widely used electrochemical energy storage (EES) devices for portable electronics due to their high energy density [1]. Nevertheless, their applicability to electric vehicle is hindered by the inability to increase the energy density beyond the intercalation of one lithium ion per transition metal or anodes alternative to graphite with appropriate redox voltages. Electrode materials based on alloying [2] as well as those based on displacement or conversion reactions [3] have opened new possibilities, but so far high power and stable cycling has not been achieved. While emerging battery technologies can benefit from the knowledge on Li-ion batteries, novel materials, purposely studied initially for other chemistries such as Mg or Na-ion batteries are also being tested back for Li-ion batteries, the benefit being mutual. Specifically, metal organic frameworks, as those of the Prussian Blue family have emerged as interesting intercalation based high power electrode materials [4].

Prussian Blue (PB), ideally $KFe_2(CN)_6 \cdot xH_2O$, is a well-known synthetic blue pigment [5]. It has a cubic lattice with a = 10.1780 Å (space group *Fm*-3*m*). In this structure, the iron atoms, Fe(II) and Fe(III), coexist on alternate corners of a small cube of 5.1 Å along the three directions of space connected by linear cyanide anions. Alkali atoms alternately occupy half of the centres of these small cubes (see Fig. 1a) [6]. Interstitial Fe^{3+} and CN vacancies are the usual defects [7].

Based on the oxidation state of the transition metal ions, PB and its transition metal substituted analogues, $KM^{II}Fe^{III}(CN)_6 \cdot xH_2O$ (PBA) [8,9] have been studied for many different properties including charge-transfer phase transitions or magnetic ordering. [10,11] Because of their large channels, they have also been tested for H_2

* Corresponding authors. CIC Energigune, Parque Tecnológico de Álava, Albert Einstein 48, Ed. CIC, 01510 Miñano, Spain.
E-mail addresses: ecastillo@cicenergigune.com (E. Castillo-Martínez), trojo@cicenergigune.com (T. Rojo).

http://dx.doi.org/10.1016/j.jpowsour.2014.08.025
0378-7753/

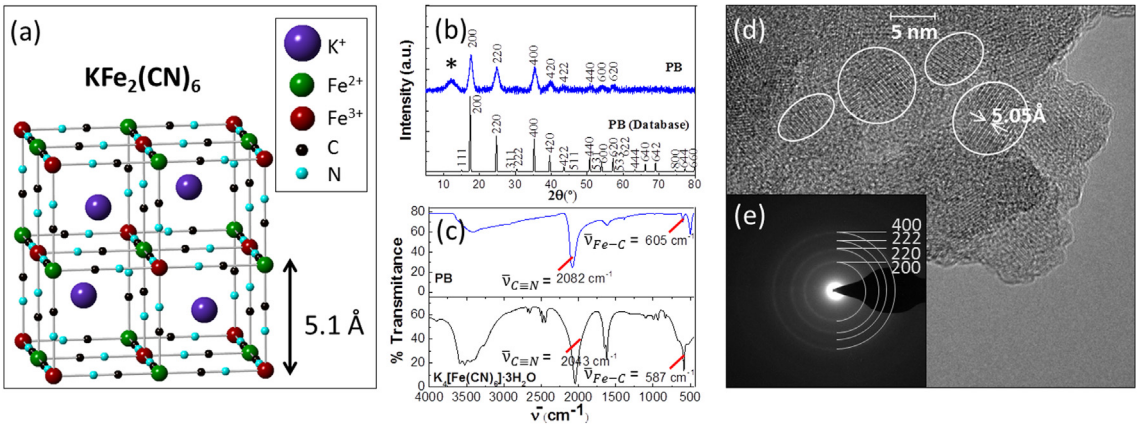

Fig. 1. a) PB structure b) XRD patterns of the PB synthesized and the PB listed in ICSD Karlsruhe Database (n° 162081). The Kapton® film peak has been marked with an *. c) IR spectra of PB and the starting reagent, $K_4[Fe(CN)_6]\cdot 3H_2O$, labelling the characteristic C≡N and Fe−C≡N absorption bands of both. d) TEM image of PB domains and e) electron diffraction pattern of PB nanocrystals with crystallographic planes indexed.

and CO_2 storage and separation [12–14] in their dehydrated state as well as for ^{137}Cs decontamination [15,16]. Interestingly, with the combination of the transition metals redox properties along with the large available tunnels for ion diffusion, PBA also display an attractive electrochemical behaviour, [17–21] which has been recently exploited in the field of electrochemical energy storage. In this sense, $KMFe(CN)_6\cdot xH_2O$ (M = Ni, Cu) have shown reversible capacities of ~50 mAh g^{-1} with the insertion of Li^+, Na^+, NH_4^+ or K^+ in aqueous electrolyte, at very high charge and discharge rates of 1 A g^{-1} at ~1 V vs NHE. [2,9,22,23] Divalent cations, such as Mg^{2+}, Ca^{2+}, Sr^{2+} and Ba^{2+}, have also been inserted into the Ni based PBA. [24] Moreover, a 0.95 V full PBA based cell, with Cu-PBA as positive- and Mn-PBA as negative-electrode materials, has recently demonstrated to deliver 28 mAh g^{-1} at 1C with no capacity loss for 1000 cycles [25].

Additionally, $KMFe(CN)_6\cdot xH_2O$ (M = Mn, Fe, Co, Ni and Zn) are also active as cathodes for Na^+ and Li^+ insertion/de-insertion in organic electrolyte. Reversible capacities of ~100 mAh g^{-1} were exhibited for M = Fe when tested versus Na^+, [26] and good performance was also observed when $AMn[Fe(CN)_6]_{0.83}\cdot 3.5H_2O$ (A = Li^+, Na^+) is cycled both versus sodium and lithium. [27] Recently high quality crystals of $NaFe_2(CN)_6$ have shown capacities above 150 mAh g^{-1} vs Na [28].

In alkali-ion batteries, PBAs have been mainly studied as positives. Interestingly, Sung Y-E and coworkers, as well as Zhang et al., have recently reported the electrochemical properties of PBA based on Co and Mn as negative for Li-ion batteries. Their experiments with Co-based PBA showed that this material can deliver reversible capacities of 400 mAh g^{-1} in the 0.01–3.0 V range [29,30].

In this paper we report on the electrochemical performance of nanosized Prussian Blue, $K_{0.88}Fe_{2.04}(CN)_6\cdot yH_2O$, as negative (indifferently called anode hereafter) for Li-ion batteries in organic electrolytes in the low voltage 0.005–1.6 V range, which enables high voltage full cells to be prepared. Iron being the only transition metal in the compound it represents the lower cost member of the PBA family. We also present insights on the possible mechanism of the alkali ion storage in this compound.

2. Experimental

2.1. Synthesis

2.1.1. PB synthesis

All chemicals were of analytical reagent and ACS grade and were used without further purification. The preparation of PB is straightforward: 100 mL of a freshly prepared pale yellow $K_4[Fe(CN)_6]\cdot 3H_2O$ 40 mM aqueous solution was mixed with 100 mL of a yellow–orange $FeCl_3\cdot 6H_2O$ 40 mM aqueous solution, using deionized water in both cases. [31] As soon as the two solutions came in contact, a blue ink colour suspension containing PB was formed in excess of potassium ions according to the reaction of Equation (1). The small PB particles resisted centrifugation at 4000 rpm during 10 min and it was necessary to force its precipitation by adding ethanol. Then, after 48 h filtering, washing with ethanol (3 × 10 mL), and drying, dark blue crystal-like aggregates of "soluble" [21] PB, actually $K_{0.88}Fe_{2.04}(CN)_6\cdot yH_2O$, were formed.

$$(1 + (x/3))\ FeCl_3 + K_4[Fe(CN)_6] \rightarrow K_{1-x}\ Fe^{III}{}_{1+(x/3)}[Fe^{II}(CN)_6]\cdot yH_2O\downarrow + (3 + x)\ KCl \quad (1)$$

2.1.2. PW synthesis

Prussian White was synthesized via solvothermal method, following the recipe described by Jiang. [32] In brief, $K_4[Fe(CN)_6]$ (1.05 mmol) added into deaerated distilled water (25 mL), was transferred into a Teflon-lined stainless autoclave, sealed in an Argon filled glove bag and then maintained at 160 °C for 48 h. After the reaction was completed, the precipitate was collected by filtration, washed several times with distilled water and acetone, and finally dried in a vacuum oven at 60 °C for 12 h.

2.2. Structural characterization

PXRD data were collected in a Bruker D8 Advance X-Ray diffractometer, with $\lambda_{CuK\alpha}$ = 1.54056 Å. The measured data range extends from 5° to 80°, 2θ, with a step width of 0.0194°. IR spectra were recorded in the range of $\bar{\nu}$ = 4000–450 cm^{-1} in transmission mode in a Perkin Elmer FTIR Spectrum 400 DTGS spectrophotometer by preparing KBr pellets. High Resolution Transmission Electron Microscopy (HRTEM) images, EDX spectra and electron diffraction patterns were recorded using a FEI Tecnai F20 S-TWIN electron microscope operated at an accelerating voltage of 200 kV equipped with an EDX spectrometer. Scanning Electron Microscopy (SEM) was utilized to study the morphology and contrast of pristine and cycled material. SEM was performed in a FEI Quanta 200F SEM operated at 30 kV and equipped with an Apollo 10 SSD Energy Dispersive X-ray (EDX) and Scanning Transmission Electron Microscopy (STEM) STEM-II detectors. Elemental analysis (H, C, N) has been performed in a Euro Elemental Analyser (CHNS), to check the

H, C and N percentage present in the sample. TGA NETZSCH STA 449 F3 Jupiter was used to collect the thermogravimetric curves. Experiments were performed in the temperature range from 30 to 325 °C using N_2 atmosphere and a temperature step of 10 K min^{-1}.

2.3. Electrochemical characterization

The electrochemical behaviour of PB was tested against lithium using a battery and cell test equipment (MACCOR Series 4000 Battery Tester). Galvanostatic measurements between 0.005 V and 1.6 V were conducted at room temperature, using two-electrode coin-type half cells (CR2032). The PB electrodes were prepared by mixing PB with amorphous carbon (super C-65) and polyvinylidene fluoride (PvdF) dissolved in *N*-methylpyrrolidone in a 80:10:10 ratio, and finally laminating the slurry on Cu foil and drying under vacuum at 80 °C overnight. Lithium metal was used as counter and reference electrodes. A glass fibre filter paper (Whatman, GF-B) impregnated with commercial (Solvionic) $LiPF_6$ 1 M in ethylene carbonate:dimethyl carbonate (EC:DMC) was used as separator. The current density was fixed at the following C-rates: 20C, 10C, 2C, C, C/10 and C/100, based on a theoretical capacity of $C_{PB,th} = 87.5$ mAh g^{-1} corresponding to the insertion of 1 Li^+/f.u. Typical cell loadings were 2–6 mg of active material per coin cell and reported data are single run for typical results.

2.4. Solubility study of cyanides in electrolyte

To check the solubility of PB, FTIR spectra of fresh electrolyte ($LiPF_6$ 1 M EC:DMC), electrolyte in contact with PB and the glass fibre of a fully discharged battery of PB were collected. All FTIR spectra were recorded using NaCl pellets and nujol in a wavelength range from 2500 to 750 cm^{-1}.

To test PB solubility in the electrolyte, ca. 30 mg of PB was added to 3 ml in $LiPF_6$ 1 M EC:DMC in a glass vial, stirred and the solid is let to settle overnight. Then, FTIR spectrum of the solution was collected.

On the other hand, to prove the formation of soluble cyanide salts accompanying the reduction of PB on the electrolyte ($LiPF_6$ 1 M EC:DMC), a few drops of DMC were added to the glass fibre separator of a completely discharged battery. It was let to settle overnight in an eppendorf and then FTIR of the solution was collected.

3. Results and discussion

3.1. PXRD, IR, TEM, HCN analysis, TGA

The formation of PB is confirmed by powder X-ray diffraction (XRD) (see Fig. 1b). Fig. S1 shows the Rietveld refinement of the XRD data with space group *Fm*-3*m* and lattice parameter $a = 10.19(2)$ Å. A crystallite size of 6.5 nm can be deduced from the refinement of the XRD data using the instrumental resolution file.

The IR spectrum of PB (Fig. 1c) exhibits the Fe–CN vibration at 605 cm^{-1} and the strong characteristic –C≡N stretching vibration at 2082 cm^{-1} ($\nu_{(C\equiv N)}$), which is shifted with regard to the cyanide band position of the starting reagent $K_4[Fe(CN)_6]\cdot 3H_2O$, that appears at 2043 cm^{-1}. [33] Moreover, the IR spectrum reveals that there is no residual EtOH from washing the material since no C–H vibration bands are observed.

TEM has been used to further characterize the resulting PB. HRTEM images show the presence of ≈5 nm PB crystalline domains which is in agreement with the particle size deduced from the refinement. These nanoparticles exhibit lattice fringes of 5.05 Å (Fig. 1d) corresponding to a half of the unit cell ($a = 10.19$ Å). The rings in the diffraction pattern fit to the main crystallographic planes of the PB structure: 200, 220, 222 and 400 (Fig. 1e). Prussian Blue's EDX semi-quantitative analysis yields a chemical formula ca. $KFe_2(CN)_6$, assuming a C/N ratio of one. As a consequence of making the analysis using a lacey carbon film on which the particles are held, the carbon signal is enhanced and only the nitrogen signal can be quantified as coming from PB. In addition, the presence of low residual chlorine (Cl) is detected (Cl:K ≤ 0.1). The latter let us assert that the product obtained was PB and not a chlorine containing derivative, as for example $K_2Fe_2(CN)_6Cl\cdot yH_2O$ (Fig. S2).

Elemental analysis (H, C, N) of the sample confirms a C/N ratio of 1.02, as expected. On the other hand, the percentage of H corresponds to $7.2H_2O$/f.u.

To calculate the interstitial and removable water content, thermogravimetric curves up to the decomposition temperature, ~325 °C are collected. Two different losses are observed at 80 °C and 125 °C corresponding to $1H_2O$ and $1.73H_2O$ molecules which could be physisorbed and zeolitic water, respectively. [34] This represents a lower content of water than the calculated from elemental analysis, that could be due to the coordinated water, which evolves only with the decomposition not being considered by TGA.

3.2. Electrochemical performance

The electrochemical performance of iron PB was tested against lithium in the 0.005–1.6 voltage range by using two-electrode coin-type half cells (CR2032) and $LiPF_6$ 1 M in EC:DMC 50:50 w/w as electrolyte.

Fig. 3a shows the first galvanostatic discharge profiles of PB vs Li at different C-rates (20C, 10C, 2C, C, C/10 and C/100, with $C_{PB,th} = 87.5$ mA g^{-1} corresponding to the insertion of 1 Li^+/f.u.). The discharge capacity is higher at low currents, as expected. However, this trend is not followed at C/100, maybe due to the electrolyte degradation, as it took one month for the battery to

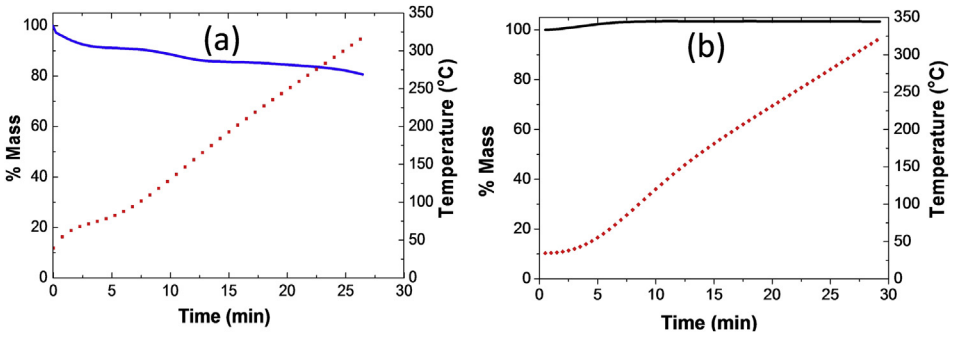

Fig. 2. Thermogravimetric analysis of pristine PB (a) and Prussian White (b), scanned from 30 to 325 °C using N_2 atmosphere and a temperature step of 10 K min^{-1}.

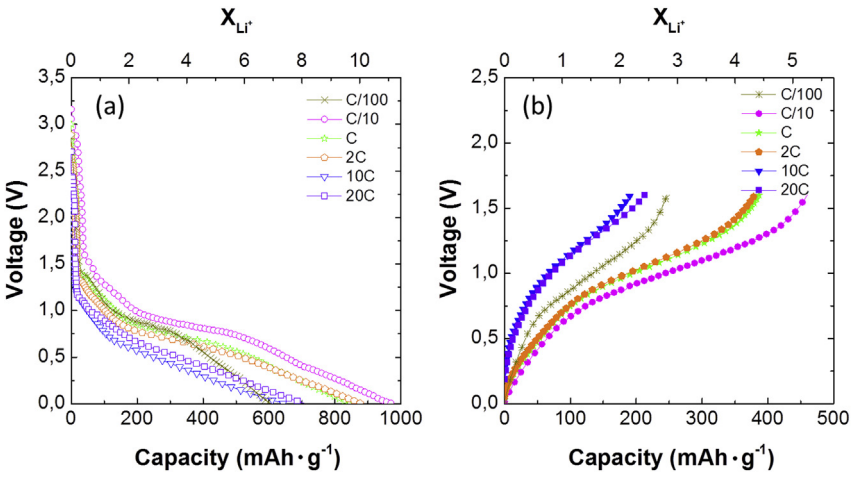

Fig. 3. Galvanostatic first discharge (a) and first charge (b) curves of PB/Li cells measured at different currents (from C/100 = 0.875 mA g^{-1} to 20C = 1.750 A g^{-1}) in the voltage range 0.005–1.6 V.

complete its first discharge. There are several redox processes between 0.1 and 1.5 V with a couple of pseudo-plateaus between 0.8 and 0.9 V which are clearly observed at low (C/100 and C/10 (8.75 mA g^{-1})) and moderate (C (87.50 mA g^{-1}) and 2C) rate capabilities but fade out at higher C-rates. The first discharge varies between 600 and 1000 mAh g^{-1} depending on the C-rate and, despite the large irreversibility of the first discharge, the material possesses fairly good reversible capacity of up to 450 mAh g^{-1} at C/10 in the first charge (see Fig. 3b). Even at high current densities, 20C (1.75 A g^{-1}), the first cycle reversible capacity is as high as 200 mAh g^{-1}, which makes it a good candidate as anode for lithium ion power batteries.

Furthermore, the PB displays a nice cyclability with a hysteresis of ca. 0.5 V as observed in Fig. 4a, reversibly inserting and de-inserting about 5 Li^+/formula unit. Although as expected, the reversible capacity increases when the C-rate decreases (Fig. 4b), the capacity retention (Fig. 4c) does not follow the same tendency. After 100 cycles all batteries show between 50 and 60% of capacity retention, which is still far from ideal. For all the tested currents, a very large irreversible capacity in the first cycle is noted due to the formation of SEI layer. It is only after 20 cycles, that the coulombic efficiency reaches 98–100%, indicating that a stable SEI has been formed.

Comparable high capacities have only been reported by Sung and Zhang, on Co-based PBA which was cycled in the 0.01–3.0 V range voltage window [29,30]. No insights into the possible mechanism of reaction were given by Sung while Zhang suggested the formation of Co^I once the cell is completely discharged, following the mechanism proposed by Cui for Mn-PBA as anode in an aqueous electrolyte battery [25].

The large reversible capacity showed by the PB, ca. 450 mAh g^{-1}, cannot be explained only by the intercalation mechanism of 1 or 2 Li^+ atoms and Fe(I) coordinated by CN ligand is not reported (≠Mn, Co). Intercalation and accompanying reduction of Fe is known to occur at voltages between 2.0 and 4.3 V vs lithium or sodium with a reversible capacity of 100–170 mAh g^{-1} [26–28,34]. Therefore, it seems very likely that a displacement or conversion reaction is taking place at voltages below 2 V, as it has been observed for many metal organic framework based materials [35].

In order to understand if this could be responsible for the observed electrochemical behaviour, ex-situ XRD and IR data of cycled electrodes after stopping and opening them at different stages of the first discharge and charge were collected (Fig. 5).

The XRD data of the initial PB electrode (Fig. 5b.i) exhibits the most intense reflections of PB (at 2θ = 17.41, 24.72, 35.24 and 39.57°). When the electrode is reduced only to 1.6 V (Fig. 5b.ii), no clear structural changes are observed as PB is expected to have all iron reduced to Fe^{2+} while keeping the structure. However, once it is fully discharged down to 0.005 V (Fig. 5b.iii), all reflections belonging to the PB disappear whereas another, corresponding to $LiPF_6$ from evaporation of imbibing solvent for the *ex-situ* observation, appears at 2θ = 25.14°. This suggests cleavage of the

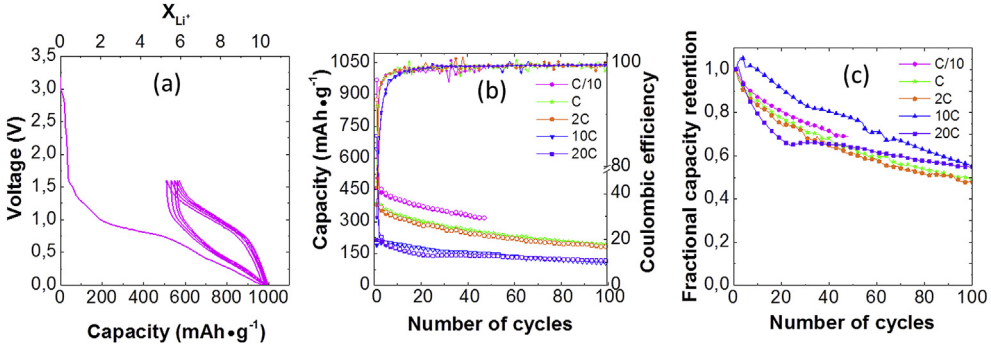

Fig. 4. Electrochemical performance of PB when tested vs lithium with $LiPF_6$ 1 M in EC:DMC. a) Voltage profile during the five first cycles of galvanostatic discharge and charge at C/10. b) Specific capacity of PB at different C-rates and their coulombic efficiency. c) Capacity retention vs cycle number for different C-rates.

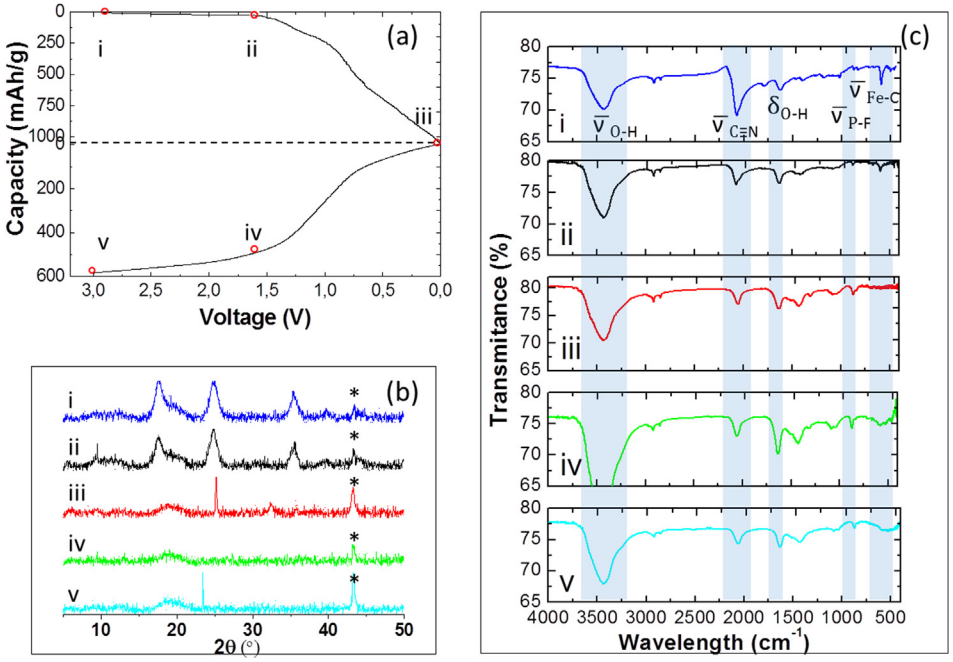

Fig. 5. a) First discharge and charge profile of PB/Li cell at R.T. in a voltage range of 0.005–3.2 V. b) XR diffractograms of the electrodes in the different points (i, ii, iii, iv, v) of the galvanostatic curve of a. The reflections due to the Cu-foil are marked with an *. c) IR spectra of the electrodes in the different points (i, ii, iii, iv, v) of the galvanostatic curve (a).

crystalline lattice which occurs in displacement reactions [36]. In addition, new reflections at 32.5 and 35.7° can be guessed in the completely discharged electrode (Fig. 5b.iii). Following the hypothesis of the displacement reaction occurring, these peaks can be attributed to the formation of Fe_2O_3 during the eventual sample exposure to air while collecting XRD, as a result of the oxidation of nanometric metallic Fe that would have been formed along the reduction process. During the following charge up to 1.6 V (Fig. 5b.iv) there is only a broad band at $2\theta = 19.41°$, assigned to the Kapton® protection. Finally, the diffractogram from the fully charged cell (Fig. 5b.v) displays a new reflection due to KPF_6 which suggests that Li^+ has replaced K^+ in the oxidized electrode and the latter was fed in the electrolyte. The absence of additional reflections indicates that the Prussian Blue long range structure is not restored.

The FTIR spectra of the electrodes shown in Fig. 5c demonstrate the presence of absorption bands corresponding to the stretching of hydroxyl ($\bar{\nu}_{\mathbf{O-H}}$), cyanide ($\bar{\nu}_{\mathbf{C\equiv N}}$), P–F bonds ($\bar{\nu}_{\mathbf{P-F}}$) and Fe–CN bonds ($\bar{\nu}_{\mathbf{Fe-CN}}$), as well as the bending of hydroxyl ($\delta_{\mathbf{O-H}}$), that are highlighted with shading. When the electrode gets discharged, the intensity of the cyanide band decreases and it is partially recovered once it is fully charged. If the reduction in intensity of this band was related to the cleavage of C≡N, the 2080 cm^{-1} absorption band would disappear, which is not the case. Besides, the sharp Fe–C band from the Fe–C≡N bond at 592 cm^{-1} disappears when the electrode is reduced and reappears as a broad band when it gets oxidized again. Since the Fe–C bond breaks while the C≡N bond remains, other metal cyanide, likely LiCN or KCN, must be forming and the reduction of intensity of the CN band could be due to the partial solubility of LiCN or the formed cyanide in the electrolyte. LiCN is a highly covalent compound with low lattice energy, hence easy to solubilize (see Supplementary data for further discussion). Comparison of FTIR spectra of fresh electrolyte, electrolyte in contact with PB and the glass fibre of a fully discharged battery of PB confirm this hypothesis (see Fig. 6).

Fig. 6a shows the FTIR spectrum of the commercial electrolyte, $LiPF_6$ 1 M EC:DMC. While the FTIR of the electrolyte that has been mixed with PB (Fig. 6b) displays no trace of the C≡N band and a very similar profile to the one obtained for the pure electrolyte, C≡N vibrations are clearly observed at 2188 and 2076 cm^{-1} in the FTIR spectra of DMC in contact with the glass fibre separator of a discharged battery (Fig. 6c). Therefore, we can state that PB is not soluble in $LiPF_6$ 1 M EC:DMC and that the discharge products have higher solubility in the electrolyte than PB. Despite having CN^- ions in solution, the basicity of the electrolyte under these reducing conditions prevent the evolution of HCN.

Besides the confirmation of a different cyanide being formed, SEM-STEM and bright field TEM images of the same electrode material after reduction down to 5 mV (Figs. 7 and 8) demonstrate the presence of bright and dark nanoparticles, respectively, which could be ascribed to metallic iron containing nanoparticles. By SEM-STEM

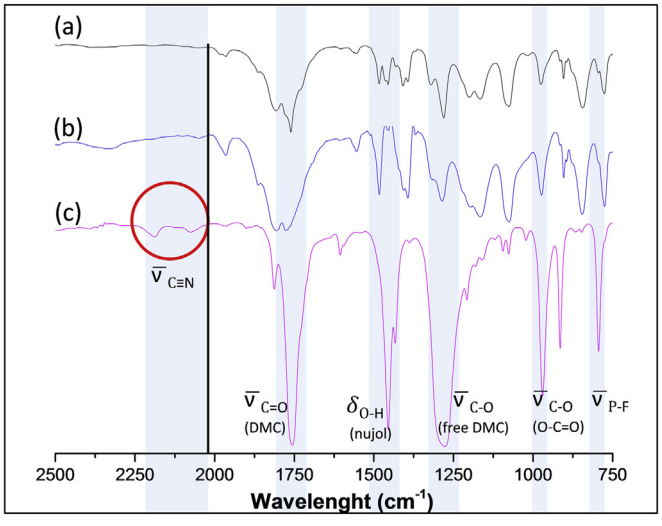

Fig. 6. FTIR spectra of a) the electrolyte ($LiPF_6$ 1 M EC:DMC), b) the electrolyte in contact with PB and c) the glass fibre of a fully discharged battery washed with DMC.

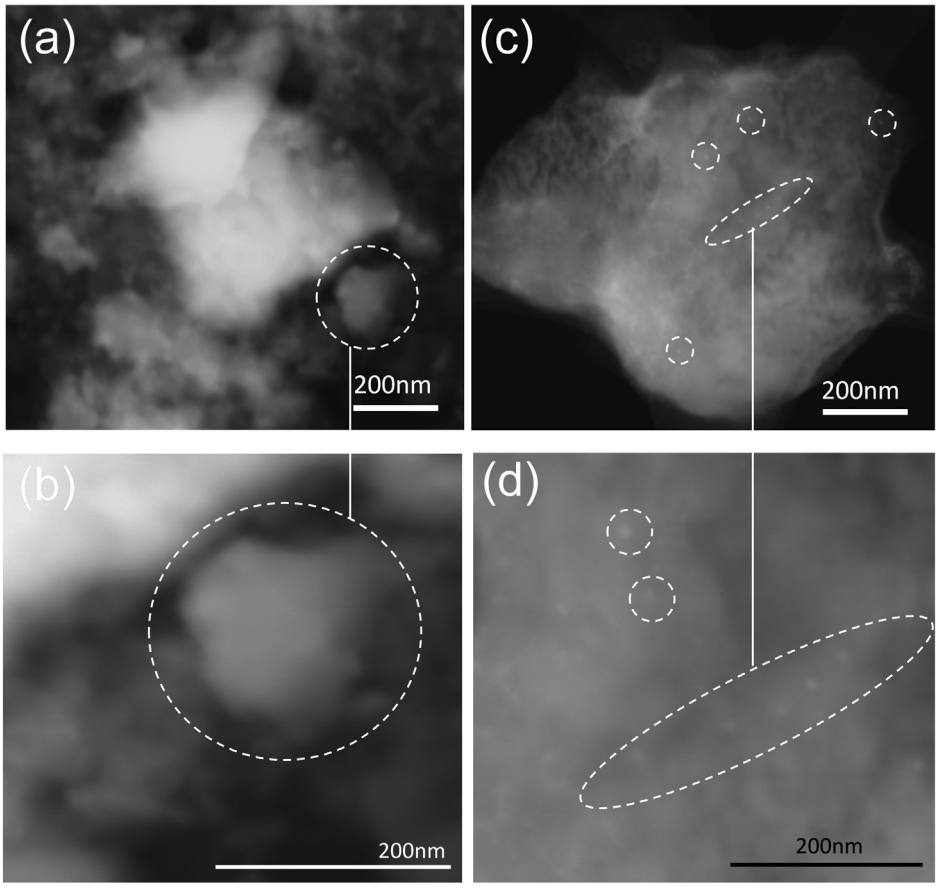

Fig. 7. SEM–STEM images of the pristine material (a) the material completely discharged (c) and zoomed zones of both of them, respectively (b, d).

microscopy, it is possible to obtain images in which the contrast is directly related to the atomic number (*Z*). The STEM images of the pristine material (Fig. 7a, b) shows a more homogeneous contrast all along the particles which represents a more homogeneous iron distribution. On the other hand, in the discharged electrodes (Fig. 7c, d), it is possible to observe bright spots (marked by dashed circles) within a darker matrix, which are related to Fe containing nanoparticles formed during the discharge process, which are not observed in the pristine electrodes (Fig. 7a, b).

These iron containing nanoparticles can also be observed in bright field TEM, but in this case as very small dark nanoparticles (of ca. 5 nm) (Fig. 8a). In Fig. 8b, the darker domains (Fig. 8b) can be assigned to elemental Fe, since the 2.1 Å interplanar distance could belong to the (1 1 1) lattice plane, as observed in Fig. 8e. Likewise, the interplanar spacings of 3.9 Å, observed as weak contrast within the matrix, could be allotted to the (2 0 0) crystallographic plane of KPF_6 (Fig. 8d) or to the (0 0 2) of Li_2O_2, whereas 3.4 Å could be assigned to the (0 1 1) of LiCN or KOH (Fig. 8c), although Li_2O_2 is unlikely to form in such reducing conditions. In Fig. 8f, the domains allocations have been done again based on the interplanar distances measured and how they coincided with the different compounds listed as possible components of the matrix. In agreement with these TEM images, the electron diffraction pattern (Fig. 8g) is composed of rings, as corresponding to nanoparticles whose distances can be allotted to the interplanar spacings of metallic Fe (2.1 Å) and KCN or KOH. To summarize the information obtained by TEM, it can be concluded that interplanar spacing close to those of metallic Fe (2.1 Å) are found in these particles (Fig. 8e). These nanoparticles are embedded into a matrix of less crystalline material which shows interplanar distances that could belong to KOH, KCN, Li_2O_2 or LiF (Fig. 8c, d, e, f, g).

Based on the above PXRD, FTIR, SEM and TEM experiments on cycled electrodes, the idea of a displacement reaction is reinforced. The proposed mechanism thought to take place during discharge involves the complete reduction of $Fe^{III/II}$ into metallic Fe^0 nanoparticles along with an unrecoverable loss of structure of PB with Fe–C bond cleavage and possible formation of Li–CN bond (in the form of LiCN) or Li–O bond (in the form of LiOH) that compose an amorphous matrix. In addition, K^+ from the PB structure may also form the corresponding potassium salts. Upon reoxidation, some Fe–C≡N or Fe–O bonds seem to be formed, justifying the stable capacity. The suggested reduction reaction is described in Equation

$$K_{1-x}Fe^{III}_{1+(x/3)}Fe^{II}(CN)_6\cdot yH_2O \xrightarrow[+(1+(x/3))e^-]{+(1+(x/3))Li^+} Li_{1+(x/3)}K_{1-x}Fe^{II}_{2+(x/3)}(CN)_6\cdot yH_2O \xrightarrow[+2\cdot(2+(x/3))e^-]{+2\cdot(2+(x/3))Li^+} (2+(x/3))Fe^0 + (5+x)LiZ + (1-x)KZ(Z = CN-, OH-, F-, \ldots) \quad (2)$$

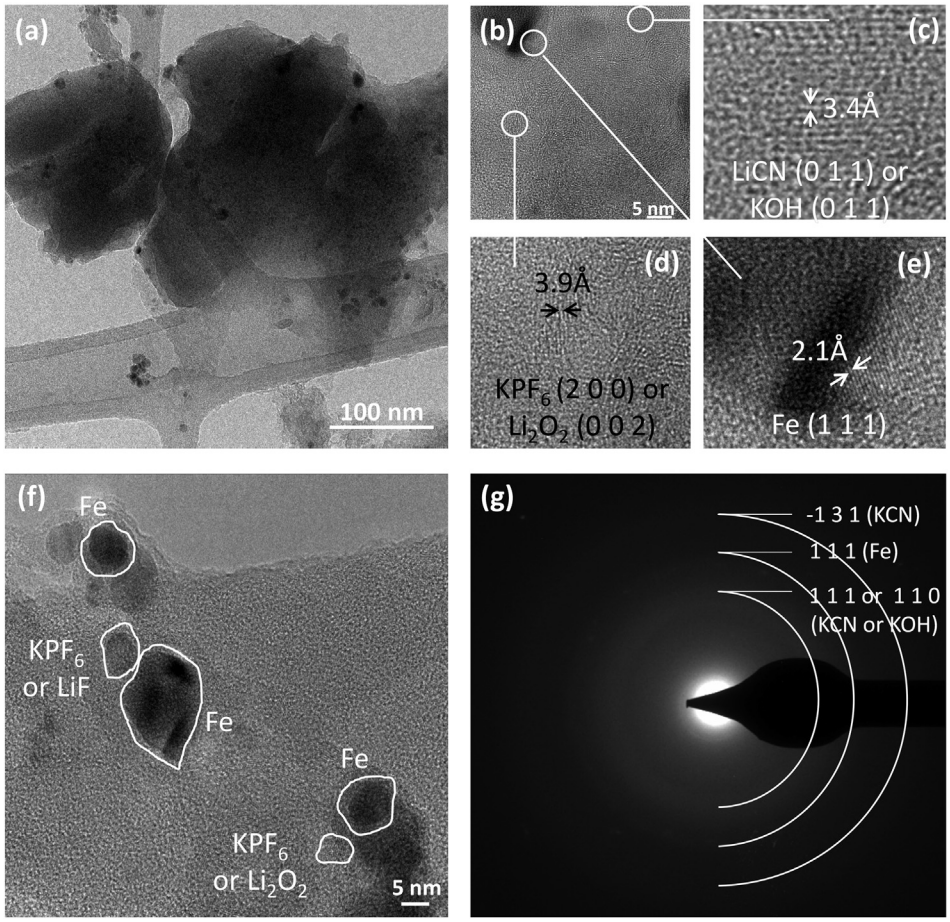

Fig. 8. a)TEM image of the material from a fully discharged half battery. b) TEM image of a completely discharged battery displaying several domains and their higher magnification (c, d and e). f) Different domains observed in a completely discharged battery, possibly containing Fe, LiF and KPF_6. g) Electron diffraction pattern of another area of the same fully discharged battery. White lines schematically indicate the broad diffraction rings with the crystallographic planes of possible reaction compounds.

(2), being $x = 0.12$, as shown by the results of Atomic Absorption Spectroscopy (AAS).

Since bands due to OH are quite intense in the IR spectra, we wondered if water plays a major role in the electrochemical performance. Previous studies revealed that hydration affects the activation energy of alkali ions diffusion, such as Li^+, $Na^{+\cdot}$ or Mg^{2+}, improving its diffusion and interfacial transfer into the PB structure and resulting in a high power output [37]. Nevertheless, the reasoning behind it only applies to measurements in aqueous media. On the other hand, the presence of water has also been shown to be beneficial and even necessary for reactions in organic media. In the case of the performance of PB as positive, removal of zeolitic water by heating up to 150 °C have little effect on the electrochemistry [34]. However coordinating water molecules, that will be lost at higher temperatures, are necessary for lithium intercalation into PB affecting strongly its electrochemical behaviour. This is also the case for the reversible Mg^{2+} electrochemical surface reaction in layered vanadium oxides [38,39].

To test the role of water in PB measured as anode in organic media, Prussian White (PW) $K_2Fe_2(CN)_6$ was synthesized as the completely reduced form of PB [32], with no zeolitic water present in the channels, as confirmed by TGA (Fig. 2b). Electrochemical measurements on PW were done in the same conditions than for PB, exhibiting similar capacities and capacity retention than that obtained for PB (Fig. S4). This seems to indicate that the presence of zeolitic water is not playing an important role in Li^+ diffusion, as previously suggested. However, the larger particle size of PW could also be affecting the electrochemical performance and therefore the measurements are not directly comparable.

Once the use of PB as anode in lithium ion battery has shown to be successful, and given the already demonstrated performance of PB as cathode, a full cell based on the use of PB for both active electrodes in organic electrolyte is conceived. We will report it in a separate communication.

4. Conclusions

In summary, the PB nanoparticles have been synthesized by an easy, economical and scalable method. The electrochemical performance of PB as anode has been tested vs Li in a half cell exhibiting reversible capacities of 400 mAh g^{-1} at C/10 (8.75 mA g^{-1}) in the first 5 cycles and 150 mAh g^{-1} stable at 20C (1750 mA g^{-1}) for 100 cycles in the narrow and low potential range from 0.005 to 1.6 V. This low voltage range means high energy density when used in a full cell. The disappearance of the PB reflections in ex-situ XRD data of reduced electrodes along with the loss of the Fe–CN infrared band suggest that this large capacity is due to the insertion of Li^+ via displacement instead of an intercalation process, involving the Fe–C bond cleavage. Additionally SEM and TEM images and diffraction suggest the presumable formation of Fe^0 nanoparticles along with cyanide salts partially soluble in the electrolyte. Therefore, the use of PB as anode in lithium ion battery has shown to be successful and the

testing of a full cell based on the use of PB for both active electrodes can be envisaged.

Acknowledgements

This work was financially supported by CICEnergiGUNE Research Centre (Etortek 10 CICEnergigune) and the Basque Government. SGIker technical and human support (UPV/EHU, MICINN, GV/EJ, ESF) is gratefully acknowledged because of the help with AAS and the elemental analysis (H, C, N). The authors would also like to acknowledge Egoitz Martín for his help with XRD data collection. Mª José Piernas Muñoz thanks the Basque Government the grant corresponding to "Nuevas Becas y renovaciones para el Programa Predoctoral de Formación de Personal Investigador".

Appendix A. Supplementary data

Supplementary data related to this article can be found at http://dx.doi.org/10.1016/j.jpowsour.2014.08.025.

References

[1] J.B. Goodenough, K.-S. Park, J. Am. Chem. Soc. 135 (2013) 1167–1176.
[2] U. Kasavajjula, C. Wang, A.J. Appleby, J. Power Sources 163 (2007) 1003–1039.
[3] J. Cabana, L. Monconduit, D. Larcher, M.R. Palacín, Adv. Energy Mater. 22 (2010) E170–E192.
[4] C.D. Wessells, R.A. Huggins, Y. Cui, Nat. Commun. 2 (2011) 550.
[5] N.N. Greenwood, A. Earnshow, Chemistry of the Elements, p. 1094 (Chapter 25).
[6] J.F. Keggin, F.D. Miles, Nature (1936) 577.
[7] H.J. Buser, D. Schwarzenbach, W. Petter, A. Ludi, Inorg. Chem. 16 (1977) 2704.
[8] D.B. Brown, D.F. Shriver, Inorg. Chem. 8 (1969) 37.
[9] C.D. Wessells, S.V. Peddada, M.T. McDowell, R.A. Huggins, Y. Cui, J. Electrochem. Soc. 159 (2012) A98–A103.
[10] H. Tokoro, S.-I. Ohkoshi, Dalton Trans. 40 (2011) 6825.
[11] W.R. Entley, G.S. Girolami, Inorg. Chem. 49 (2010) 1524–1534.
[12] S.S. Kaye, J.R. Long, J. Am. Chem. Soc. 127 (2005) 6506–6507.
[13] S. Natesakhawat, J.T. Culp, C. Matranga, B. Bockrath, J. Phys. Chem. C 111 (2007) 1055–1060.
[14] R.K. Motkuri, P.K. Thallapally, B.P. McGrail, S.B. Ghorishi, Cryst. Eng. Commun. 12 (2010) 4003–4006.
[15] N.L. Torad, M. Hu, M. Imura, M. Naito, Y. Yamauchi, J. Mater. Chem. 22 (2012) 18261–18267.
[16] M. Ishizaki, S. Akiba, A. Ohtanj, Y. Hoshi, K. Ono, M. Matsuba, T. Togashi, K. Kananizuka, M. Sakamoto, A. Takahashi, T. Kawamoto, H. Tanaka, M. Watanabe, M. Arisaka, T. Nankawa, M. Kurihara, Dalton Trans. 42 (2013) 16049–16055.
[17] V.D. Neff, J. Electrochem. Soc. 125 (1978) 886.
[18] V.D. Neff, J. Electrochem. Soc. 132 (1985) 6.
[19] D. Ellis, M. Eckhoff, V.D. Neff, J. Phys. Chem. 85 (1981) 1225.
[20] K. Itaya, H. Akahoshi, S. Toshima, J. Electrochem. Soc. 129 (1982) 1498–1500.
[21] K. Itaya, I. Uchida, Acc. Chem. Res. 19 (1986) 162–168.
[22] A. Widmann, H. Kahlert, I. Petrovic-Prelevic, H. Wulff, J.V. Yakhmi, N. Bagkar, F. Scholz, Inorg. Chem. 41 (2002) 5706.
[23] C.D. Wessells, S.V. Peddada, R.A. Huggins, Y. Cui, Nano Lett. 11 (2011) 5421.
[24] R.Y. Wang, C.D. Wessells, R.A. Huggins, Y. Cui, Nano Lett. 13 (2013) 5748–5752.
[25] M. Pasta, C.D. Wessells, N. Liu, J. Nelson, M.T. McDowell, R.A. Huggins, M.F. Toney, Y. Cui, Nat. Commun. 5 (2014), http://dx.doi.org/10.1038/ncomms4007.
[26] Y. Lu, L. Wang, J. Cheng, J.B. Goodenough, Chem. Commun. 48 (2012) 6544–6546.
[27] T. Matsuda, M. Takachi, Y. Moritomo, Chem. Commun. 49 (2013) 2750–2752.
[28] Y. You, X.-L. Wu, Y.-X. Yin, Y.-G. Guo, Energy Environ. Sci. 7 (2014) 1643–1647.
[29] M. Shokouhimehr, S.-H. Yu, D.-C. Lee, D. Ling, T. Hyeon, Y.-E. Sung, Nanosci. Nanotechnol. Lett. 5 (7) (2013) 770–774.
[30] P. Nie, L. Shen, H. Luo, B. Ding, G. Xu, J. Wang, X. Zhang, J. Mater. Chem. A 2 (2014) 5852–5857.
[31] H.B. Weiser, W.O. Milligan, J.B. Bates, J. Phys. Chem. B 46 (1942) 99–111.
[32] M. Hu, J.S. Jiang, Mater. Res. Bull. 46 (2011) 702–707.
[33] L. Xia, R.L. McCreery, J. Electrochem. Soc. 146 (1999) 3696–3701.
[34] N. Imanishi, T. Morikawa, J. Kondo, Y. Takeda, O. Yamamoto, N. Kinugasa, T. Yamagishi, J. Power Sources 79 (1999) 215–219.
[35] P. Tran-Van, K. Barthelet, M. Morcrette, M. Herlem, J.-M. Tarascon, A.K. Cheetham, Gérard Férey, J. New Mater. Electrochem. Syst. 6 (2003) 29–31.
[36] H. Li, P. Balaya, J. Maier, J. Electrochem. Soc. 151 (2004) A1878–A1885.
[37] Y. Mizuno, M. Okubo, E. Hosono, T. Kudo, H. Zhow, K. Oh-ishi, J. Phys. Chem. C 117 (2013) 10877–10882.
[38] P. Novak, W. Scheifele, O. Haas, J. Power Sources 54 (1995) 479.
[39] P. Novak, W. Scheifele, F. Joho, O. Haas, J. Electrochem. Soc. 142 (1995) 2544.